Journal of Computational and Applied Mathematics 291 (2016) 209–224

Contents lists available at ScienceDirect

Journal of Computational and Applied Mathematics

journal homepage: www.elsevier.com/locate/cam

Stability of differentially heated flow from a rotating sphere

S.J.D. D'Alessio [a,*], N. Leung [b], J.W.L. Wan [c]

[a] Department of Applied Mathematics, University of Waterloo, Waterloo, Ontario, N2L 3G1, Canada
[b] Department of Computer Science, University of Toronto, Toronto, Ontario, M5S 2J7, Canada
[c] Cheriton School of Computer Science, University of Waterloo, Waterloo, Ontario, N2L 3G1, Canada

HIGHLIGHTS

- Differentially heated flow of a thin fluid layer from a rotating sphere has been investigated.
- A numerical solution procedure for solving the steady and unsteady equations has been proposed.
- An approximate analytical solution has been derived.
- A linear stability analysis has estimated a theoretical value for the onset of instability.
- Good agreement was found between numerical, analytical and theoretical results.

ARTICLE INFO

Article history:
Received 9 October 2014
Received in revised form 9 March 2015

Keywords:
Rayleigh–Bénard convection
Rotation
Thin flow
Analytical
Numerical
Stability

ABSTRACT

We present results on the flow of a thin fluid layer over a rotating sphere having a surface temperature that varies in the latitudinal direction. The fluid is taken to be viscous, incompressible and Newtonian while the flow is assumed to possess both azimuthal and equatorial symmetry. The governing Navier–Stokes and energy equations are formulated in terms of a stream function and vorticity and are solved subject to no-slip boundary conditions. An approximate analytical solution for the steady-state flow has been derived and is compared with numerical solutions to the steady and limiting unsteady equations. For small Rayleigh numbers these solutions are found to be in close agreement. However, as the Rayleigh number is increased noticeable differences occur. A numerical solution procedure is presented and a linear stability analysis has been conducted to predict the onset of instability. Good agreement between the theoretical predictions and the observed numerical simulations was found.

1. Introduction

The flow and heat transfer of a thin fluid layer from a differentially heated rotating sphere are of interest in geophysical and meteorological applications such as weather prediction and climate modelling [1,2]. Differential heating and rotation combined with stratification of the fluid layer make this a challenging problem. One goal of this research is to present a simple mathematical model to describe such flows; another is to construct numerical and analytical solution procedures to solve this problem. A compact mathematical model together with an efficient solver can be used as a platform to explore and better understand model sensitivity to physical processes and discretization [3]. It can also be used to examine, evaluate, and when necessary, revise parameterizations that are currently used in weather forecasting and climate modelling to describe key unresolved sub-grid processes [4].

* Corresponding author. Tel.: +1 519 888 4567x35014.
E-mail addresses: sdalessio@uwaterloo.ca (S.J.D. D'Alessio), natleung@cs.utoronto.ca (N. Leung), jwlwan@cs.uwaterloo.ca (J.W.L. Wan).

http://dx.doi.org/10.1016/j.cam.2015.03.025
0377-0427/

Some previous related studies include Marcus and Tuckerman [5,6] who carried out numerical simulations of the flow between two concentric differentially rotating spheres in the absence of heating. In this case the flow is analogous to Taylor–Couette flow [7] whereby Taylor vortices resembling Hadley cells can form. Hart, Glatzmaier and Toomre [8], on the other hand, presented three-dimensional numerical simulations of thermal convection in a rotating hemispherical shell and presented a thorough summary of earlier investigations. The research carried out by Lesueur et al. [9] numerically investigated the flow in a thick spherical shell using parameters that are consistent with those of the outer planets. The fluid was subjected to both internal and external heat sources with the external source representing solar heating. The flow pattern consisted of two Hadley cells on each side of the equator extending from the equator to the poles occupying the entire fluid layer.

Regarding the stability of the flow, one of the earliest works can be attributed to Chandrasekhar [10] who formulated the problem using a spherical shell geometry. Walton [11] extended the classical Rayleigh–Bénard problem [12–14] to include a slowly varying temperature along the bottom plate. His analysis showed that a slowly varying temperature has a stabilizing effect on the flow and hence delays the onset of instability. In this research we have applied his analysis to our problem. Later, Soward and Jones [15] analytically investigated the stability of the isothermal flow in the narrow gap between two concentric differentially rotating spheres. The more recent work of Lewis and Langford [16] blends bifurcation theory and computations to examine the stability of differentially heated flow from a rotating sphere. Their calculations showed that as the equator-to-pole temperature difference increases from zero, large Hadley cells extending from the equator to poles form immediately. As the temperature difference increases two or three convection cells appear in each hemisphere. A related problem involves the stability of a boundary layer on a rotating sphere. Barrow, Garrett and Peake [17] and Garrett and Peake [18], among others, have solved the stability problem for the case of a sphere rotating in a fluid which is otherwise at rest.

Although this study tackles a problem that has been addressed by several researchers, the adopted approach is significantly different. Key differences lie in the mathematical formulation of the problem as well as the numerical and analytical solution procedures. The paper is structured as follows. In Section 2 we present the governing equations and the corresponding initial and boundary conditions. Following that, in Section 3, we conduct a linear stability analysis to estimate the onset of instability. This involves deriving an approximate analytical solution to the steady-state equations which is then fed into the stability analysis. The numerical solution procedure for solving both the steady and unsteady equations is outlined in Section 4. The numerical and analytical results are presented and discussed in Section 5. The investigation is summarized in the concluding section. Lastly, an Appendix A is included to provide more details on the mathematical formulation of the problem.

2. Governing equations

The atmosphere can be thought of as a thin fluid layer covering the surface of a rotating sphere. Based on this a simple mathematical model describing the unsteady laminar convective flow of a viscous incompressible dry Boussinesq fluid from a solid impermeable rotating differentially heated sphere can be formulated. The flow domain and configuration are illustrated in Fig. 1. In the rotating reference frame the fluid is taken to be initially at rest and is then set into motion by buoyancy as a result of a prescribed poleward decrease in surface temperature as well as a radial decrease in temperature. The poleward decrease in surface temperature mimics solar heating and is taken to be sinusoidal since this is consistent with the amount of solar radiation penetrating into the surface as it tilts away from the equator. In addition, the flow is assumed to possess both azimuthal and equatorial symmetry.

Owing to the assumed symmetry, the unsteady Navier–Stokes equations can be expressed in terms of a stream function, ψ, scaled vorticity, ω, and scaled zonal velocity, W. Appendix A presents the primitive formulation of the problem in terms of the velocity components v_r, v_θ, v_ϕ and pressure P, and also explains how the equations for ψ, ω and W can be obtained. In spherical coordinates (r, θ, ϕ) and cast in dimensionless form the governing Navier–Stokes and energy equations can be expressed as

$$\omega = -\delta D^2\psi, \tag{1}$$

$$\frac{\partial\omega}{\partial t} + \frac{\delta}{r^2\sin\theta}\frac{\partial(\psi,\omega)}{\partial(\theta,r)} + \delta\, Pr\, Ra\sin\theta\frac{\partial T}{\partial\theta} + \frac{2\delta\omega}{r^2\sin^2\theta}\left(\cos\theta\frac{\partial\psi}{\partial r} - \frac{\sin\theta}{r}\frac{\partial\psi}{\partial\theta}\right) - \left(\frac{2\delta^2 W}{r^2\sin^2\theta} + \frac{2\delta^2}{Ro}\right)\left(\cos\theta\frac{\partial W}{\partial r} - \frac{\sin\theta}{r}\frac{\partial W}{\partial\theta}\right) = \delta^2\, Pr\, D^2\omega, \tag{2}$$

$$\delta^2\, Pr\, D^2 W - \frac{\partial W}{\partial t} = \frac{\delta}{r^2\sin\theta}\frac{\partial(\psi,W)}{\partial(\theta,r)} - \frac{2\delta}{Ro}\left(\cos\theta\frac{\partial\psi}{\partial r} - \frac{\sin\theta}{r}\frac{\partial\psi}{\partial\theta}\right), \tag{3}$$

$$\frac{\partial T}{\partial t} + \frac{\delta}{r^2\sin\theta}\frac{\partial(\psi,T)}{\partial(\theta,r)} = \delta^2\nabla^2 T. \tag{4}$$

As noted in the Appendix A, the key underlying assumptions and approximations made in deriving Eqs. (1)–(4) include: the Boussinesq approximation, ignoring the variation in the gravitational acceleration with radial distance from the surface, and assuming that the rate of rotation is sufficiently small that the centrifugal acceleration, and its impact on pressure, can be

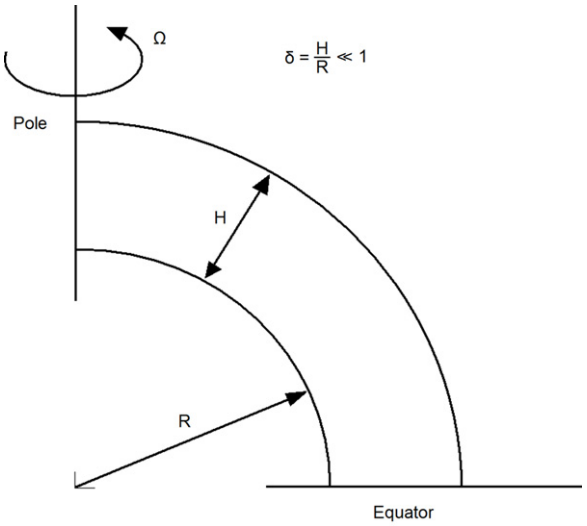

Fig. 1. The flow set up.

neglected. In the above t denotes time, r is the radial coordinate, and θ is the angle with the polar axis. The variable T denotes the scaled temperature. The dimensionless parameters appearing in the above equations include the Rayleigh number (Ra), the Rossby number (Ro), the Prandtl number (Pr) and the shallowness parameter (δ) which are defined as follows:

$$Ra = \frac{\alpha g_0 H^3 \Delta T}{\nu\kappa}, \qquad Ro = \frac{\kappa}{H\Omega R}, \qquad Pr = \frac{\nu}{\kappa}, \qquad \delta = \frac{H}{R}.$$

Here, the fluid properties ν, κ and α represent the kinematic viscosity, thermal diffusivity and thermal expansion coefficient, respectively, whereas g_0 is the acceleration due to gravity, R is the radius of the sphere, H is the thickness of the fluid layer, ΔT is the temperature scale, and Ω is the rotation rate about the polar axis. The time and length are scaled according to

$$\tilde{t} \to \frac{H^2}{\kappa} t, \qquad \tilde{r} \to Rr,$$

while the adopted scaling for the flow variables is given by

$$(\tilde{\psi}, \tilde{\omega}, \tilde{W}) \to \left(\frac{\kappa R^2}{H}\psi, \frac{\kappa R}{H^2}\omega, \frac{\kappa R}{H} W\right),$$

where the tilde denotes a dimensional quantity. We present the scaling of the temperature in more detail. As in the study by Lewis and Langford [16], the surface temperature is allowed to vary sinusoidally. In dimensional form we have

$$\tilde{T} = T_{ave} - \Delta T \cos(2\theta),$$

with T_{ave} denoting the average surface temperature. Along the top of the fluid layer we impose a constant temperature of T_{edge}. Then we define the scaled temperature as

$$T = \frac{\tilde{T} - T_{edge}}{T_{ave} + \Delta T - T_{edge}}.$$

Lastly, the differential operators D^2, ∇^2 and $\partial(A, B)/\partial(x, y)$ are defined as follows:

$$D^2 = \frac{\partial^2}{\partial r^2} + \frac{1}{r^2}\frac{\partial^2}{\partial\theta^2} - \frac{\cot\theta}{r^2}\frac{\partial}{\partial\theta},$$
$$\nabla^2 = \frac{\partial^2}{\partial r^2} + \frac{2}{r}\frac{\partial}{\partial r} + \frac{1}{r^2}\frac{\partial^2}{\partial\theta^2} + \frac{\cot\theta}{r^2}\frac{\partial}{\partial\theta},$$
$$\frac{\partial(A, B)}{\partial(x, y)} = \frac{\partial A}{\partial x}\frac{\partial B}{\partial y} - \frac{\partial A}{\partial y}\frac{\partial B}{\partial x}.$$

Eqs. (1)–(4) are to be solved in the region

$$0 \le \theta \le \frac{\pi}{2}, \qquad 1 \le r \le 1 + \delta,$$

subject to the no-slip and impermeability boundary conditions

$$\psi = \frac{\partial \psi}{\partial r} = W = 0 \quad \text{on } r = 1 \text{ and } r = 1 + \delta.$$

The assumed symmetry requires that we impose the following conditions at the pole and equator

$$\psi = \omega = W = 0 \quad \text{along } \theta = 0 \quad \text{and} \quad \psi = \omega = \frac{\partial W}{\partial \theta} = 0 \quad \text{along } \theta = \frac{\pi}{2}.$$

We observe that the stream function is overspecified while the vorticity is underspecified. Later we will explain how the extra conditions for the stream function can be used to furnish the missing conditions for the vorticity. In dimensionless form the temperature is taken to satisfy

$$T = 1 - \gamma \cos^2 \theta \quad \text{on } r = 1 \quad \text{and} \quad T = 0 \quad \text{on } r = 1 + \delta, \tag{5}$$

where

$$\gamma = \frac{2\Delta T}{T_{ave} + \Delta T - T_{edge}},$$

and represents the ratio of the maximum surface temperature difference to the maximum difference in temperature between the surface and the top of the fluid layer. Hence, the temperature has been scaled so that the maximum temperature difference between the surface and the top of the fluid layer is unity, and the constant temperature at the top of the fluid layer is zero. At the pole ($\theta = 0$) and the equator ($\theta = \pi/2$) we apply the zero heat-flux (i.e. Neumann) condition

$$\frac{\partial T}{\partial \theta} = 0 \quad \text{along } \theta = 0 \text{ and } \theta = \frac{\pi}{2}. \tag{6}$$

In solving the unsteady problem we assume that the fluid is initially at rest having a temperature distribution given by the approximate analytical solution derived in the next section.

3. Linear stability analysis

For analytical and numerical purposes we propose a change of coordinates and introduce (z, μ) where $r = 1 + \delta z$ and $\mu = \cos\theta$. This has the advantage of mapping the computational domain to the unit square: $0 \le z, \mu \le 1$. On the unit square, the transformed equations read

$$\delta\omega = -\hat{D}^2\psi, \tag{7}$$

$$\begin{aligned}
&\frac{\partial \omega}{\partial t} + \frac{1}{(1+\delta z)^2}\frac{\partial(\psi,\omega)}{\partial(z,\mu)} + \frac{2\omega}{(1-\mu^2)(1+\delta z)^2}\left[\mu\frac{\partial\psi}{\partial z} + \frac{\delta(1-\mu^2)}{(1+\delta z)}\frac{\partial\psi}{\partial\mu}\right] \\
&\quad - \frac{2\delta W}{(1-\mu^2)(1+\delta z)^2}\left[\mu\frac{\partial W}{\partial z} + \frac{\delta(1-\mu^2)}{(1+\delta z)}\frac{\partial W}{\partial\mu}\right] - \frac{2\delta}{R_0}\left[\mu\frac{\partial W}{\partial z} + \frac{\delta(1-\mu^2)}{(1+\delta z)}\frac{\partial W}{\partial\mu}\right] \\
&\quad = \delta\, Pr\, Ra(1-\mu^2)\frac{\partial T}{\partial\mu} + Pr\,\hat{D}^2\omega,
\end{aligned} \tag{8}$$

$$\frac{\partial T}{\partial t} + \frac{1}{(1+\delta z)^2}\frac{\partial(\psi,T)}{\partial(z,\mu)} = \hat{\nabla}^2 T, \tag{9}$$

$$Pr\,\hat{D}^2 W - \frac{\partial W}{\partial t} = \frac{1}{(1+\delta z)^2}\frac{\partial(\psi,W)}{\partial(z,\mu)} - \frac{2}{R_0}\left[\mu\frac{\partial\psi}{\partial z} + \frac{\delta(1-\mu^2)}{(1+\delta z)}\frac{\partial\psi}{\partial\mu}\right]. \tag{10}$$

The transformed differential operators become

$$\hat{D}^2 = \frac{\partial^2}{\partial z^2} + \frac{\delta^2(1-\mu^2)}{(1+\delta z)^2}\frac{\partial^2}{\partial\mu^2},$$

$$\hat{\nabla}^2 = \frac{\partial^2}{\partial z^2} + \frac{2\delta}{(1+\delta z)}\frac{\partial}{\partial z} - \frac{2\mu\delta^2}{(1+\delta z)^2}\frac{\partial}{\partial\mu} + \frac{\delta^2(1-\mu^2)}{(1+\delta z)^2}\frac{\partial^2}{\partial\mu^2}.$$

For small δ approximate analytical solutions can be constructed by expanding the flow variables in the following series:

$$\psi = \psi_0 + \delta\psi_1 + \delta^2\psi_2 + \cdots,$$
$$\omega = \omega_0 + \delta\omega_1 + \delta^2\omega_2 + \cdots,$$
$$W = W_0 + \delta W_1 + \delta^2 W_2 + \cdots,$$
$$T = T_0 + \delta T_1 + \delta^2 T_2 + \cdots.$$

Using the above expansions it is a straight-forward exercise to show that

$$\psi_0 = \psi_1 = \omega_0 = W_0 = W_1 = 0,$$

as well as to determine the non-zero terms $\psi_2, \omega_1, \omega_2, W_2, T_0, T_1$ and T_2. For the steady-state equations the approximate solutions, correct to second order in δ, are given by

$$\psi_s(z,\mu) \approx -2\gamma\delta^2 Ra\,\mu(1-\mu^2)F_1(z),$$
$$\omega_s(z,\mu) \approx 2\gamma\delta\, Ra\,\mu(1-\mu^2)\left[\frac{d^2F_1}{dz^2} + \delta F_2(z)\right],$$
$$W_s(z,\mu) \approx \frac{4\gamma\delta^2\, Ra}{Pr\, R_0}\mu^2(1-\mu^2)F_3(z),$$
$$T_s(z,\mu) \approx (1-\gamma\mu^2)(1-z)(1-\delta z) + \delta^2 T_2(z,\mu),$$

where

$$F_1(z) = \frac{z^4}{24} - \frac{z^5}{120} - \frac{7z^3}{120} + \frac{z^2}{40},$$
$$F_2(z) = \frac{z^4}{12} - \frac{z^3}{6} + \frac{z}{12} - \frac{1}{60},$$
$$F_3(z) = \frac{z^5}{120} - \frac{z^6}{720} - \frac{7z^4}{480} + \frac{z^3}{120} - \frac{z}{1440},$$
$$\begin{aligned} T_2(z,\mu) \;=\; & \gamma(1-3\mu^2)z^2\left(1-\frac{z}{3}\right) + (1-\gamma\mu^2)z^2\left(1-\frac{z^2}{3}\right) + \gamma^2\, Ra\,\mu^2(1-\mu^2)z^3 \\ & \times\left(\frac{z^4}{252} - \frac{z^3}{36} + \frac{41z^2}{600} - \frac{3z}{40} + \frac{1}{30}\right) - \gamma\, Ra(1-3\mu^2)(1-\gamma\mu^2)z^4\left(\frac{z^2}{360} - \frac{z^3}{2520} - \frac{7z}{1200} + \frac{1}{240}\right) \\ & + z\left(-\frac{2}{3}(1-\gamma\mu^2) - \frac{2}{3}\gamma(1-3\mu^2) - \frac{1}{350}\gamma^2\, Ra\,\mu^2(1-\mu^2) + \frac{1}{1400}\gamma\, Ra(1-3\mu^2)(1-\gamma\mu^2)\right). \end{aligned}$$

These approximate analytical solutions will next be used to conduct a linear stability analysis. Later, these approximate analytical solutions will also be used to validate the steady-state numerical solutions as well as the limiting unsteady numerical solutions for large t.

To investigate the stability of the steady-state flow we begin by perturbing the flow by imposing a small disturbance and monitoring how the disturbance evolves in time. We set

$$T = T_s + T', \qquad \psi = \psi_s + \psi', \qquad \omega = \omega_s + \omega', \qquad W = W_s + W',$$

where T', ψ', ω', W' denote disturbances. Substituting these into the governing equations and linearizing we obtain the following system of perturbation equations

$$\delta\omega' = -\hat{D}^2\psi', \tag{11}$$
$$\hat{\nabla}^2 T' = \frac{1}{(1+\delta z)^2}\left(\frac{\partial(\psi_s, T')}{\partial(z,\mu)} + \frac{\partial(\psi', T_s)}{\partial(z,\mu)}\right), \tag{12}$$
$$\begin{aligned} & Pr\,\hat{D}^2\omega' + \delta\, Pr\, Ra(1-\mu^2)\frac{\partial T'}{\partial\mu} \\ & = \frac{1}{(1+\delta z)^2}\left(\frac{\partial(\psi_s,\omega')}{\partial(z,\mu)} + \frac{\partial(\psi',\omega_s)}{\partial(z,\mu)}\right) + \frac{2\omega_s}{(1-\mu^2)(1+\delta z)^2}\left(\mu\frac{\partial\psi'}{\partial z} + \frac{\delta(1-\mu^2)}{(1+\delta z)}\frac{\partial\psi'}{\partial\mu}\right) \\ & \quad + \frac{2\omega'}{(1-\mu^2)(1+\delta z)^2}\left(\mu\frac{\partial\psi_s}{\partial z} + \frac{\delta(1-\mu^2)}{(1+\delta z)}\frac{\partial\psi_s}{\partial\mu}\right) - \frac{2\delta W_s}{(1-\mu^2)(1+\delta z)^2}\left(\mu\frac{\partial W'}{\partial z} + \frac{\delta(1-\mu^2)}{(1+\delta z)}\frac{\partial W'}{\partial\mu}\right) \\ & \quad - \frac{2\delta W'}{(1-\mu^2)(1+\delta z)^2}\left(\mu\frac{\partial W_s}{\partial z} + \frac{\delta(1-\mu^2)}{(1+\delta z)}\frac{\partial W_s}{\partial\mu}\right) - \frac{2\delta}{R_0}\left(\mu\frac{\partial W'}{\partial z} + \frac{\delta(1-\mu^2)}{(1+\delta z)}\frac{\partial W'}{\partial\mu}\right), \end{aligned} \tag{13}$$
$$Pr\,\hat{D}^2 W' = \frac{1}{(1+\delta z)^2}\left(\frac{\partial(\psi_s, W')}{\partial(z,\mu)} + \frac{\partial(\psi', W_s)}{\partial(z,\mu)}\right) - \frac{2}{R_0}\left(\mu\frac{\partial\psi'}{\partial z} + \frac{\delta(1-\mu^2)}{(1+\delta z)}\frac{\partial\psi'}{\partial\mu}\right). \tag{14}$$

In arriving at (11)–(14) we have made use of the principle of exchange of stabilities [13] which is expected to hold. This allows us to ignore derivatives with respect to time at the threshold of instability.

Following Walton [11], we next expand the disturbances in powers of δ:

$$T'(z,\mu) = (T^{(0)}(z,\mu) + \delta T^{(1)}(z,\mu) + \delta^2 T^{(2)}(z,\mu) + \cdots) \exp\left(\frac{i}{\delta}\int_0^\mu k(\xi)d\xi\right),$$

$$\psi'(z,\mu) = (\psi^{(0)}(z,\mu) + \delta \psi^{(1)}(z,\mu) + \delta^2 \psi^{(2)}(z,\mu) + \cdots) \exp\left(\frac{i}{\delta}\int_0^\mu k(\xi)d\xi\right),$$

$$\omega'(z,\mu) = (\omega^{(0)}(z,\mu) + \delta \omega^{(1)}(z,\mu) + \delta^2 \omega^{(2)}(z,\mu) + \cdots) \exp\left(\frac{i}{\delta}\int_0^\mu k(\xi)d\xi\right),$$

$$W'(z,\mu) = (W^{(0)}(z,\mu) + \delta W^{(1)}(z,\mu) + \delta^2 W^{(2)}(z,\mu) + \cdots) \exp\left(\frac{i}{\delta}\int_0^\mu k(\xi)d\xi\right).$$

As noted in [11], the above correspond to disturbances having a wavenumber, $k(\mu)$, that are slowly varying as a result of the variation in the boundary condition for the surface temperature. Further, we expand the Rayleigh number and differential operators in similar series

$$Ra = Ra^{(0)} + \delta\, Ra^{(1)} + \delta^2\, Ra^{(2)} + \cdots,$$

$$\hat{D}^2 = \frac{\partial^2}{\partial z^2} + \delta^2(1-\mu^2)\frac{\partial^2}{\partial \mu^2} + \cdots,$$

$$\hat{\nabla}^2 = \frac{\partial^2}{\partial z^2} + 2\delta\frac{\partial}{\partial z} + \delta^2\left(-2\mu\frac{\partial}{\partial \mu} + (1-\mu^2)\frac{\partial^2}{\partial \mu^2}\right) + \cdots.$$

Substituting these into (11)–(14) leads to a hierarchy of problems. Although this can be a tedious procedure, we will see that for our purposes the leading-order problem provides a wealth of information.

The leading-order problem for W' is given by

$$\frac{\partial^2 W^{(0)}}{\partial z^2} - k^2(1-\mu^2)W^{(0)} = 0,$$

and is subject to

$$W^{(0)} = 0 \quad \text{at } z = 0,\, 1.$$

The solution to the above is the trivial solution $W^{(0)} \equiv 0$. Similarly, it follows that $\psi^{(0)} \equiv 0$. $T^{(0)}$ and $\psi^{(1)}$ satisfy the coupled system

$$\left[\frac{\partial^2}{\partial z^2} - k^2(1-\mu^2)\right] T^{(0)} = ik(1-\gamma\mu^2)\psi^{(1)},$$

$$\left[\frac{\partial^2}{\partial z^2} - k^2(1-\mu^2)\right]^2 \psi^{(1)} = ikRa^{(0)}(1-\mu^2)T^{(0)},$$

while $\omega^{(0)}$ can be found from

$$\omega^{(0)} = -\left[\frac{\partial^2}{\partial z^2} - k^2(1-\mu^2)\right]\psi^{(1)}.$$

The equations for $T^{(0)}$ and $\psi^{(1)}$ can be combined to yield

$$\left[\frac{\partial^2}{\partial z^2} - k^2(1-\mu^2)\right]^3 \psi^{(1)} = -k^2\, Ra^{(0)}(1-\mu^2)(1-\gamma\mu^2)\psi^{(1)}.$$

Now, the most unstable region occurs at the equator ($\theta = \pi/2$ or $\mu = 0$) since the temperature difference between the surface and the edge is largest. Likewise, the most stable region occurs at the pole ($\theta = 0$ or $\mu = 1$). Also, because of the assumed equatorial symmetry the maximum wavelength that the domain can support will be the pole-to-pole distance which is π. Thus, the allowable perturbation wavelengths are $\lambda_n = \pi/n$, where $n = 1, 2, 3, \ldots$ is a positive integer, and the corresponding discrete meridional perturbation wavenumbers are $k_n = 2n$. Since the disturbance will be concentrated near the equator we set $\mu = 0$ to obtain

$$\left[\frac{\partial^2}{\partial z^2} - k_0^2\right]^3 \psi^{(1)} = -k_0^2\, Ra^{(0)}\psi^{(1)}, \tag{15}$$

where $k_0 = k(0)$.

Solving (15) subject to the conditions

$$\psi^{(1)} = \frac{\partial \psi^{(1)}}{\partial z} = \left(\frac{\partial^2}{\partial z^2} - k_0^2\right)\psi^{(1)} = 0 \quad \text{at } z = 0,\, 1,$$

Table 1
Calculated values of $Ra^{(0)}$ for various values of k_0.

k_0	$Ra^{(0)}$
2	2178
4	1879
6	3418
8	7085

suggests looking for a solution of the form

$$\psi^{(1)}(z, \mu) = \hat{f}(\mu) e^{qz},$$

where q are the roots of the equation

$$(q^2 - k_0^2)^3 = k_0^2 \, Ra^{(0)}.$$

The roots are given by $\pm iq_1, \pm q_2, \pm q_2^*$ where the asterisk denotes the complex conjugate and

$$q_1 = k_0\sqrt{\beta - 1}, \qquad \text{Real}(q_2) = \frac{k_0}{\sqrt{2}} \left(\sqrt{1 + \beta + \beta^2} + 1 + \frac{\beta}{2} \right)^{1/2},$$

$$\text{Imag}(q_2) = \frac{k_0}{\sqrt{2}} \left(\sqrt{1 + \beta + \beta^2} - 1 - \frac{\beta}{2} \right)^{1/2},$$

where $\beta = (Ra^{(0)}/k_0^4)^{1/3}$. Introducing $\bar{z} = z - 1/2$ forces an even solution of the form

$$\psi^{(1)}(\bar{z}, \mu) = \hat{f}(\mu)[A \cos(q_1 \bar{z}) + B \cosh(q_2 \bar{z}) + C \cosh(q_2^* \bar{z})].$$

Applying the boundary conditions yields a homogeneous system of equations for the constants A, B, C. Setting the determinant of the coefficient matrix to zero and simplifying produces the dispersion relation

$$q_1 \tan\left(\frac{q_1}{2}\right) + \frac{(q_3 + \sqrt{3}q_4) \sinh q_3 + (\sqrt{3}q_3 - q_4) \sin q_4}{\cosh q_3 + \cos q_4} = 0,$$

where $q_3 = \text{Real}(q_2)$ and $q_4 = \text{Imag}(q_2)$. We define $Ra_{crit}^{(0)}$ as the minimum value of $Ra^{(0)}$ having a real wavenumber $k_{0,crit}$. From the allowable wavenumbers and the computed values listed in Table 1 it follows that the minimum value of $Ra^{(0)}$ occurs when $k_{0,crit} = 4$ and the numerical solution to the above algebraic equation yields $Ra_{crit}^{(0)} \approx 1879$. Hence, to leading order $Ra_{crit} \approx 1879$.

We observe that the problem bears a close resemblance to the classical Rayleigh–Bénard problem with rotation having no influence. The only differences lie in the allowable wavenumbers and the values of Ra_{crit} and k_{crit}, which assume the numerical values of 1708 and 3.12, respectively, for the Rayleigh–Bénard problem.

4. Numerical solution procedure

Eqs. (7)–(10) are solved by a finite difference method where the spatial derivatives are discretized by central differences and the time derivative by implicit time stepping [19]. Since we are working on a unit square, we take the grid spacing to be uniform in both the z and μ directions. We discretize the interior of the unit square using the grid points $z_i = ih$, $\mu_j = jk$ for $i = 1, \ldots, m_1$ and $j = 1, \ldots, m_2$, where $h = 1/(m_1 + 1)$ and $k = 1/(m_2 + 1)$ denote the uniform spacing in z and μ directions, respectively. In our numerical experiments we take $h = k$ so $m_1 = m_2 \equiv m$.

The finite difference discretization for the steady and unsteady equations results in a system of coupled discrete nonlinear equations. Let $(\psi^n, \omega^n, T^n, W^n)$ denote the numerical solution at time t_n with the initial condition at $t = t_0$ represented by $(\psi^0, \omega^0, T^0, W^0)$. At each time step, the solution at time t_{n+1}, namely $(\psi^{n+1}, \omega^{n+1}, T^{n+1}, W^{n+1})$, is computed by solving the discrete nonlinear system using fixed point iteration described below.

We take the initial guess to be

$$(\psi_0^{n+1}, \omega_0^{n+1}, T_0^{n+1}, W_0^{n+1}) = (\psi^n, \omega^n, T^n, W^n),$$

which corresponds to the solution at the previous time step, and let $(\psi_k^{n+1}, \omega_k^{n+1}, T_k^{n+1}, W_k^{n+1})$ be an approximate solution after k fixed point iterations of $(\psi^{n+1}, \omega^{n+1}, T^{n+1}, W^{n+1})$. From here the iteration procedure starts by solving Eq. (9) for T_{k+1}^{n+1} using the known value of ψ_k^{n+1}. Similarly, we solve Eq. (10) to obtain W_{k+1}^{n+1} using ψ_k^{n+1}. The boundary conditions for these two variables are handled using a standard approach, with the Neumann conditions being discretized along the corresponding boundaries.

Specifically, in the $(k + 1)$-th fixed point iteration for time t_{n+1}, we construct a matrix equation

$$(A_T)_{(k+1)}^{(n+1)} T_{k+1}^{n+1} = (b_T)_{(k+1)}^{(n+1)},$$

where, with a slight abuse of notation, T_{k+1}^{n+1} is a vectorized version of the discrete grid values of the state variable T in the $(k+1)$-th iteration at time t_{n+1}. As long as the matrix and vector orderings match, it does not matter how T is vectorized. After transforming the boundary conditions (5), (6) in terms of the coordinates (z, μ), we see that there are $m(m+1)$ unknowns for T. The size of the matrix equation for T is then $m(m+1) \times m(m+1)$. Given ψ_k^{n+1}, the interior equations on (z_i, μ_j) can be discretized as

$$\begin{aligned}
\frac{T_{k+1}^{n+1}(z_i,\mu_j) - T^n(z_i,\mu_j)}{\triangle t} &= -\frac{1}{(1+\delta z_i)^2}\left(\frac{(\psi_k^{n+1}(z_{i+1},\mu_j) - \psi_k^{n+1}(z_{i-1},\mu_j))}{2h}\frac{(T_{k+1}^{n+1}(z_i,\mu_{j+1}) - T_{k+1}^{n+1}(z_i,\mu_{j-1}))}{2k}\right.\\
&\left. - \frac{(T_{k+1}^{n+1}(z_{i+1},\mu_j) - T_{k+1}^{n+1}(z_{i-1},\mu_j))}{2h}\frac{(\psi_k^{n+1}(z_i,\mu_{j+1}) - \psi_k^{n+1}(z_i,\mu_{j-1}))}{2k}\right)\\
&+ \frac{T_{k+1}^{n+1}(z_{i+1},\mu_j) - 2T_{k+1}^{n+1}(z_i,\mu_j) + T_{k+1}^{n+1}(z_{i-1},\mu_j)}{h^2} + \left(\frac{2\delta}{1+\delta z}\right)\left(\frac{T_{k+1}^{n+1}(z_{i+1},\mu_j) - T_{k+1}^{n+1}(z_{i-1},\mu_j)}{2h}\right)\\
&- \left(\frac{2\mu\delta^2}{(1+\delta z)^2}\right)\left(\frac{T_{k+1}^{n+1}(z_i,\mu_{j+1}) - T_{k+1}^{n+1}(z_i,\mu_{j-1})}{2k}\right) + \left(\frac{\delta^2(1-\mu^2)}{(1+\delta z)^2}\right)\\
&\times \left(\frac{T_{k+1}^{n+1}(z_i,\mu_{j+1}) - 2T_{k+1}^{n+1}(z_i,\mu_j) + T_{k+1}^{n+1}(z_i,\mu_{j-1})}{k^2}\right).
\end{aligned}$$

Along the boundaries $\mu = 0, 1$ we apply the Neumann condition $\partial T/\partial\mu = 0$. Using a second-order one-sided discretization, this condition yields

$$-3T_{k+1}^{n+1}(z_i,0) + 4T_{k+1}^{n+1}(z_i,\mu_1) - T_{k+1}^{n+1}(z_i,\mu_2) = 0, \quad i = 1,2,\ldots,m$$

along $\mu = 0$ and

$$-3T_{k+1}^{n+1}(z_i,\mu_{m-2}) + 4T_{k+1}^{n+1}(z_i,\mu_{m-1}) - T_{k+1}^{n+1}(z_i,1) = 0, \quad i = 1,2,\ldots,m$$

along $\mu = 1$. The resulting (m^2+2m) equations in (m^2+2m) unknowns completely characterize the matrix $(A_T)_{(k+1)}^{(n+1)}$ and the vector $(b_T)_{(k+1)}^{(n+1)}$ in the $(k+1)$-th fixed point iteration, given ψ_k^{n+1}. Similarly, one can construct the matrix $(A_W)_{(k+1)}^{(n+1)}$ and the vector $(b_W)_{(k+1)}^{(n+1)}$.

The determination of ω_{k+1}^{n+1} and ψ_{k+1}^{n+1}, however, requires more care. We note that there are six boundary conditions for ψ and only two boundary conditions for ω. The stream function ψ has two boundary conditions at both $z = 0$ and $z = 1$, while ω has none. The lack of boundary conditions at $z = 0$ and $z = 1$ leads to an incomplete system for ω when Eq. (7) is discretized. Various methods have been advanced to deal with this. These include the use of so-called integral conditions, discretized boundary conditions based on Taylor expansions, and others [20–22].

Our strategy for solving Eqs. (7) and (8) is as follows. In the $(k+1)$-th iteration, we view these equations as a joint system, and we seek to simultaneously determine ω_{k+1}^{n+1} and ψ_{k+1}^{n+1}. For ψ we need m^2 equations because $\psi = 0$ along the boundary, whereas for ω we need (m^2+2m) equations because the values of ω are unknown along $z = 0$ and $z = 1$. Unfortunately, Eq. (8) can only produce m^2 equations. The remaining $2m$ equations are inferred from the extra boundary conditions for ψ as follows.

We extend the grid and assume that Eq. (7) holds along $z = 0$ and $z = 1$. Adopting the notation $f_{i,j} \equiv f(z_i, \mu_j)$, and discretizing Eq. (7) using central differences leads to

$$\delta\omega_{i,j} = -\frac{(\psi_{i+1,j} - 2\psi_{i,j} + \psi_{i-1,j})}{h^2} - \frac{\delta^2(1-\mu_j^2)}{(1+\delta z_i)^2}\frac{(\psi_{i,j+1} - 2\psi_{i,j} + \psi_{i,j-1})}{k^2},$$

where in our case $h = k$. Using the condition $\psi_{i,j} = \psi_{i,j\pm1} = 0$ along the boundaries $z = 0$ and $z = 1$, the above simplifies to

$$\delta\omega_{i,j} = -\frac{(\psi_{i+1,j} + \psi_{i-1,j})}{h^2}.$$

Along the line $z = 0$ the unknown $\psi_{i-1,j}$ lies outside the domain while along $z = 1$ the unknown $\psi_{i+1,j}$ lies outside the domain. These quantities can be eliminated by making use of the condition $\partial\psi/\partial z = 0$ along $z = 0$ and $z = 1$ which yields $\psi_{i-1,j} = \psi_{i+1,j}$ along these lines. Thus, the surface vorticity (i.e. $z = 0$) is given by the second-order finite-difference expression

$$\omega_{i,j} = -\frac{2\psi_{i+1,j}}{\delta h^2},$$

while on $z = 1$ the corresponding expression is

$$\omega_{i,j} = -\frac{2\psi_{i-1,j}}{\delta h^2}.$$

These expressions determine the remaining $2m$ equations. When put together, we have $(2m^2 + 2m)$ equations for the same number of unknowns. This approach results in a system that is about two times bigger than what would have been obtained if (ψ, ω) were decoupled. However, the system is still sparse, and can be solved rapidly using efficient algorithms. Therefore, given T_{k+1}^{n+1} and W_{k+1}^{n+1}, the matrix $(A_{\omega,\psi})_{(k+1)}^{(n+1)}$ and the vector $(b_{\omega,\psi})_{(k+1)}^{(n+1)}$ can be determined.

This completes one iteration of the fixed point method. Iterations are repeated until convergence is reached. The adopted stopping criterion is given by

$$\|(\psi_{k^*+1}^{n+1}, \omega_{k^*+1}^{n+1}, T_{k^*+1}^{n+1}, W_{k^*+1}^{n+1}) - (\psi_{k^*}^{n+1}, \omega_{k^*}^{n+1}, T_{k^*}^{n+1}, W_{k^*}^{n+1})\|_\infty < tol,$$

where the subscript ∞ denotes the infinity norm. From our experience, if the system reaches a steady state after a certain time t_n, then it typically takes only a few iterations ($k^* < 10$) to reach $tol = 10^{-6}$. When convergence is reached, we assign the converged values to be the solutions at the next time step, that is,

$$(\psi^{n+1}, \omega^{n+1}, T^{n+1}, W^{n+1}) = (\psi_{k^*+1}^{n+1}, \omega_{k^*+1}^{n+1}, T_{k^*+1}^{n+1}, W_{k^*+1}^{n+1}).$$

A complete algorithm for advancing the system from time t_n to time t_{n+1} is as follows.

Set $(\psi_0^{n+1}, \omega_0^{n+1}, T_0^{n+1}, W_0^{n+1}) = (\psi^n, \omega^n, T^n, W^n)$.
for $k = 0, 1, \ldots$ **do**
  Compute $(A_T)_{(k+1)}^{(n+1)}$ and $(b_T)_{(k+1)}^{(n+1)}$ from ψ_k^{n+1}.
  Solve

$$(A_T)_{(k+1)}^{(n+1)} T_{k+1}^{n+1} = (b_T)_{(k+1)}^{(n+1)}.$$

  Compute $(A_W)_{(k+1)}^{(n+1)}$ and $(b_W)_{(k+1)}^{(n+1)}$ from ψ_k^{n+1}.
  Solve

$$(A_W)_{(k+1)}^{(n+1)} W_{k+1}^{n+1} = (b_W)_{(k+1)}^{(n+1)}.$$

  Compute $(A_{\omega,\psi})_{(k+1)}^{(n+1)}$ and $(b_{\omega,\psi})_{(k+1)}^{(n+1)}$ from T_{k+1}^{n+1} and W_{k+1}^{n+1}.
  Solve

$$(A_{\omega,\psi})_{(k+1)}^{(n+1)} \begin{pmatrix} \omega_{k+1}^{n+1} \\ \psi_{k+1}^{n+1} \end{pmatrix} = (b_{\omega,\psi})_{(k+1)}^{(n+1)}.$$

  if $||(\psi_{k+1}^{n+1}, \omega_{k+1}^{n+1}, T_{k+1}^{n+1}, W_{k+1}^{n+1}) - (\psi_k^{n+1}, \omega_k^{n+1}, T_k^{n+1}, W_k^{n+1})||_\infty < tol$ **then**
    Break.
  end if
end for
Set

$$(\psi^{n+1}, \omega^{n+1}, T^{n+1}, W^{n+1}) = (\psi_{k+1}^{n+1}, \omega_{k+1}^{n+1}, T_{k+1}^{n+1}, W_{k+1}^{n+1}).$$

The above time stepping algorithm can be easily modified to solve the steady-state equations by simply setting the time derivatives equal to zero in Eqs. (7)–(10). Equivalently, if the numerical discretization matrices are set up just as $(A_T)_{(k+1)}^{(n+1)}$ above, then we could formally obtain the discretized steady-state linear systems by letting $\Delta t \to \infty$. We remark that when Ra exceeds Ra_{crit} the flow becomes unstable, and consequently difficulties in obtaining numerical convergence to the steady-state system may arise.

5. Results and discussion

Numerical solutions to the steady and unsteady equations have been obtained. In all of our computations we have set $\gamma = 0.5$, $Ro = 1$ and $Pr = 0.7$ (corresponding to air) and have allowed the δ and Ra to vary. The computational parameters used include $m = 80$ (i.e. 80×80 grid) implying a uniform grid spacing of $1/80$, and for the unsteady computations the uniform time step $\Delta t = 0.01$ was used. The initial conditions used in the unsteady calculations were $W = \psi = \omega = 0$ and $T = T_s(z, \mu)$.

We begin by making comparisons between the analytical and numerical steady-state solutions. Fig. 2 plots the absolute value of the maximum difference (i.e. infinity norm) between the analytical and numerical solutions for various values of δ and confirms the second-order accuracy in the approximate analytical solution.

Several grid refinement experiments were conducted in order to ensure that the adopted grid size was able to adequately resolve the flow. Table 2 lists the absolute value of the maximum difference between the analytical and numerical solutions for various values of m. Since the analytical solution is second order accurate in δ, the maximum difference will depend on both δ and m. To isolate the dependence on m we have set $\delta = 0.001$ which is small enough that the maximum difference

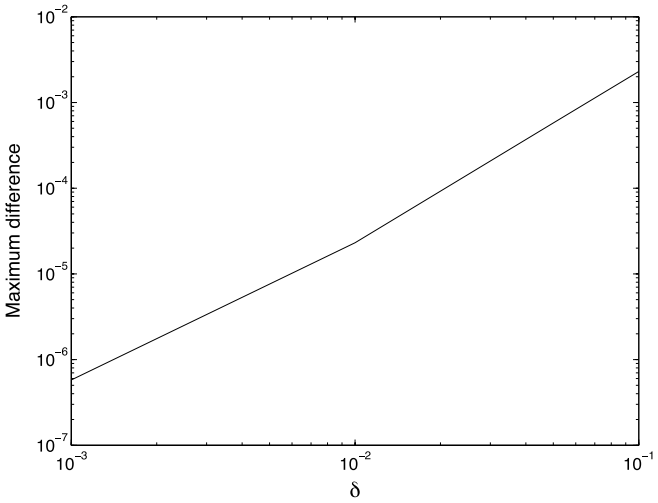

Fig. 2. Loglog plot of the maximum difference between the analytical and numerical steady-state solutions. Parameter values: $Ra = 100$, $\gamma = 0.5$, $Pr = 0.7$, $Ro = 1$.

Table 2
Maximum difference between the analytical and numerical steady-state solutions for various values of m. Parameter values: $\delta = 0.001$, $Ra = 100$, $\gamma = 0.5$, $Pr = 0.7$, $Ro = 1$.

m	Maximum difference
10	2.8×10^{-5}
20	8.2×10^{-6}
40	2.2×10^{-6}
60	1.0×10^{-6}
80	5.8×10^{-7}
100	3.7×10^{-7}

is dominated by changes in m. We see from the table that there is little change in going from an 80×80 grid to one that is 100×100. For the parameter values considered in this study an 80×80 grid was judged to be adequate.

Illustrated in Figs. 3, 4 are contour plots of the steady-state stream function in (z, μ) and Cartesian (i.e. physical) coordinates, respectively, for $Ra = 1500$. Shown along the axes in Fig. 3 are both the spherical coordinates (r, θ) as well as the (z, μ) coordinates. This serves to illustrate the nonlinear mapping between θ and μ. We note that the change of variable $\mu = \cos(\theta)$ has the property of preserving the grid spacing near the equator while stretching the grid spacing near the pole. This is precisely what is needed since the instability occurs near the equator and thus a finer grid is required there in order to resolve it. Near the pole, on the other hand, a coarser grid can be used to adequately capture the flow in that region.

The circulation pattern shows a meridional Hadley cell whereby warmer air rises at the equator, sinks at the pole and then returns to the equator to complete the counterclockwise loop. This flow pattern transports excess heat from the equator to the pole and it is seen to accomplish this through one large circulation. However, it is conceivable that for larger Ra it can achieve this more efficiently through a flow pattern consisting of two or more cells. One large Hadley cell extending from the equator to the pole was also reported in the studies of Lesueur et al. [9] and Lewis and Langford [16]. In [16] two or three convection cells were observed as the equator-to-pole temperature difference was increased.

Next we contrast the steady-state surface vorticity distribution. Plotted in Fig. 5 are the numerical and analytical solutions for $Ra = 1500$. The two solutions are seen to be in close agreement. Overall, good agreement was found between the analytical and numerical steady-state solutions in all the flow variables for Rayleigh numbers up to about 1800. In addition, for Rayleigh numbers up to about 1800 the unsteady solutions converged to the steady-state solutions.

The steady-state zonal velocity distribution is illustrated in Fig. 6 for $Ra = 1500$ and reveals a prominent westerly peak. Based on the approximate analytical solution this peak is located at $\mu = 1/\sqrt{2}$ (or $\theta = \pi/4$) and $z \approx 0.74$ or $(x, y) \approx (0.76, 0.76)$. This agrees well with the location of the peak obtained numerically which occurs at $(z, \mu) \approx (0.73, 0.73)$ or $(x, y) \approx (0.78, 0.73)$. This corresponds to a strong westerly flow which can be interpreted as the jet stream.

Lastly, Fig. 7 portrays the steady-state temperature distribution for $Ra = 1500$. As expected, the temperature decreases radially from the surface as well as latitudinally from the equator and the warmest region is concentrated along the surface near the equator. It is also clear from the diagram that the radial gradient in temperature is largest near the equator.

To numerically determine the critical Rayleigh number for the threshold of instability, Ra_{crit}, a perturbation was added to the steady-state solution and used as an initial condition which was then marched in time. By monitoring the growth or decay of the disturbance and stepping the Rayleigh number we were able to determine the interval over which the flow

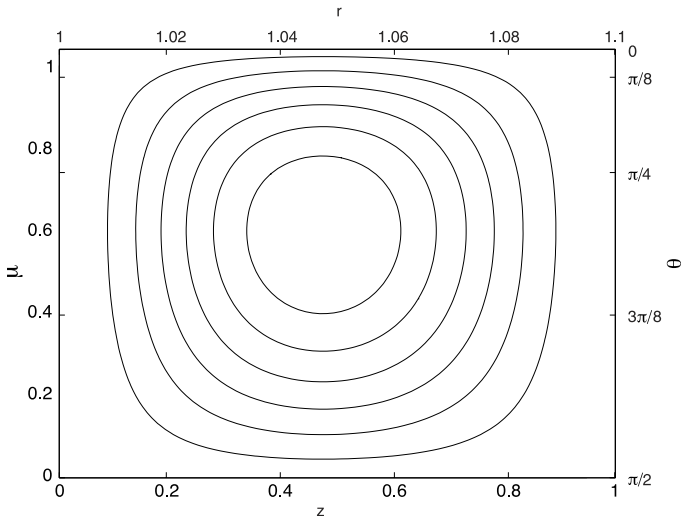

Fig. 3. Streamline circulation pattern in (z, μ) coordinates. Parameter values: $Ra = 1500$, $\delta = 0.1$, $\gamma = 0.5$, $Pr = 0.7$, $Ro = 1$.

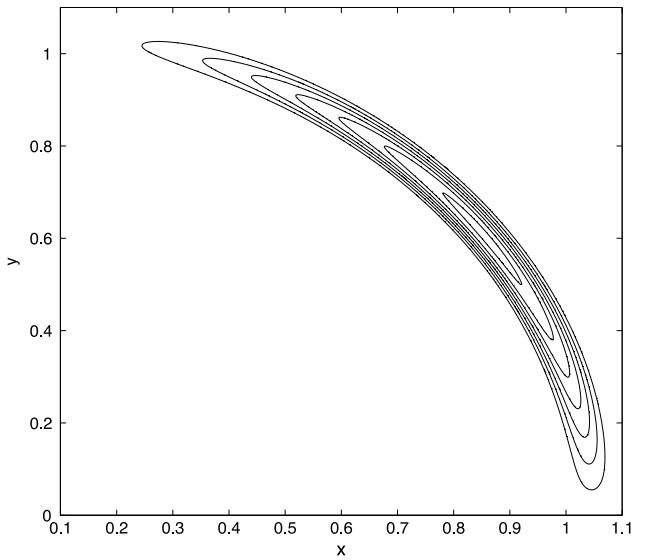

Fig. 4. Streamline circulation pattern in Cartesian coordinates. Parameter values: $Ra = 1500$, $\delta = 0.1$, $\gamma = 0.5$, $Pr = 0.7$, $Ro = 1$.

changed from being stable to becoming unstable. The perturbation for the stream function was taken to be

$$\psi' = \mu\sqrt{1-\mu^2}z^2(z-1)^2.$$

The form of the perturbation was chosen so as to satisfy all the boundary conditions. The corresponding perturbation for the vorticity was obtained by numerically solving Eq. (7). The perturbations for the other flow variables were taken to be zero. Because the stream function and vorticity are related through Eq. (7) which is independent of time, it is imperative to perturb both the stream function and vorticity in order for the effects of the perturbations to spread to the remaining equations.

We observed that as the Rayleigh number was increased beyond 1870 the unsteady solution began to show noticeable departures from the steady-state solution. The formation of a small second cell near the equator started to appear. This signals the onset of instability as predicted by the linear stability analysis. The small cell has a counterclockwise circulation as previously described while the larger cell has a clockwise circulation. Shown in Fig. 8 is a contour plot for the unsteady stream function for $Ra = 1870$ at $t = 10.6$. There was little change in the solution beyond $t = 10.6$ indicating that the solution has reached a steady state. Figs. 9–11, on the other hand, illustrate contour snapshots at times $t = 8.5$, 10.7 and 12.9, respectively, for $Ra = 1890$ and clearly show the formation of an instability and the growth in the disturbance. Thus, the flow becomes unstable in the interval $1870 < Ra < 1890$ which agrees well with our prediction $Ra_{crit} \approx 1879$.

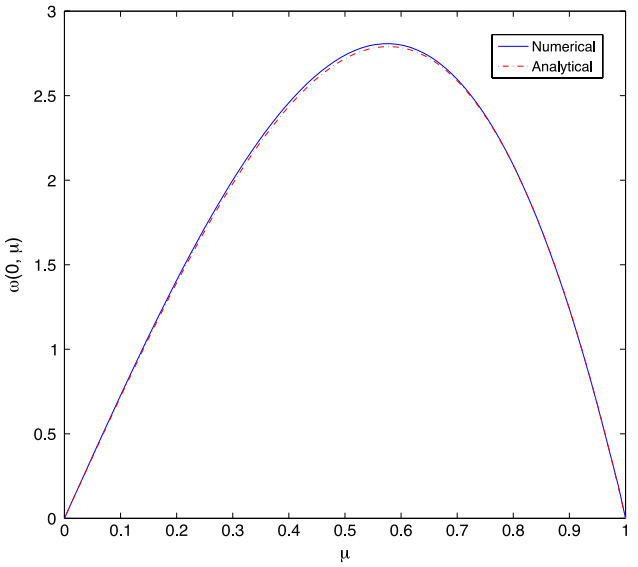

Fig. 5. Analytical (red) and numerical (blue) surface vorticity distributions. Parameter values: $Ra = 1500, \delta = 0.1, \gamma = 0.5, Pr = 0.7, Ro = 1$. (For interpretation of the references to colour in this figure legend, the reader is referred to the web version of this article.)

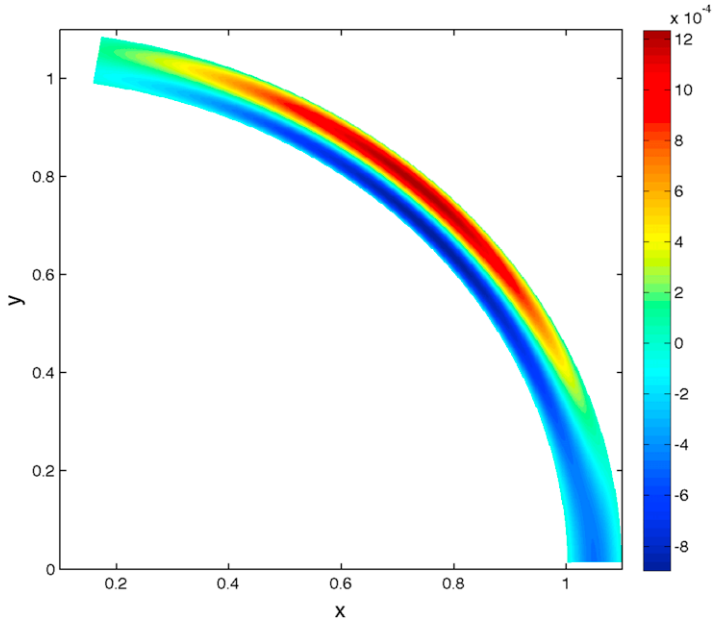

Fig. 6. The zonal velocity distribution. Parameter values: $Ra = 1500, \delta = 0.1, \gamma = 0.5, Pr = 0.7, Ro = 1$.

6. Conclusions

Discussed in this work was an analytical and numerical investigation of the differentially heated flow of a thin fluid layer over a rotating sphere. Our results revealed that for Rayleigh numbers up to 1870 good agreement exists between the analytical and numerical steady-state solutions. However, as the Rayleigh number is increased the flow becomes unstable causing noticeable differences between the steady and unsteady numerical solutions.

To leading order the stability of the flow is well approximated by that of the classical Rayleigh–Bénard problem, that is, the flow between two flat plates heated from below. This makes sense for a thin fluid layer since the flow can be approximated by a series of flat plates at each value of θ. The most unstable configuration in the series will be that at the equator, $\theta = \pi/2$, where the temperature difference is largest. The difference between the problem investigated here and the Rayleigh–Bénard problem lies in the allowed wavenumbers; here, the wavenumbers are restricted by the geometry of

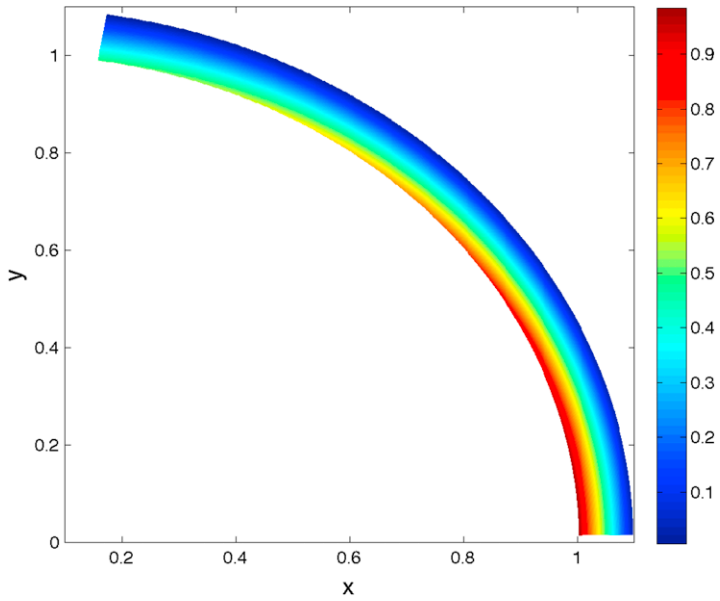

Fig. 7. The temperature distribution. Parameter values: $Ra = 1500$, $\delta = 0.1$, $\gamma = 0.5$, $Pr = 0.7$, $Ro = 1$.

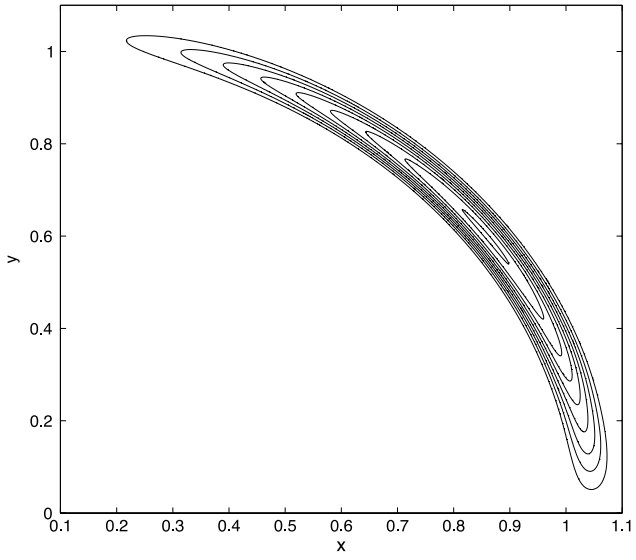

Fig. 8. Streamline circulation pattern in Cartesian coordinates at time $t = 10.6$. Parameter values: $Ra = 1870$, $\delta = 0.1$, $\gamma = 0.5$, $Pr = 0.7$, $Ro = 1$.

the domain. Good agreement was found between the theoretical prediction of the onset of instability and the observed fully nonlinear numerical simulations.

Although the presented model represents a gross simplification of the atmospheric circulation, ignoring effects such as moisture and irregularities in the surface due to topography, it is able to reproduce some key features such as the formation of Hadley cells extending from the equator to the poles and the jet stream. Future work will involve reformulating the problem with a focus on the unsteady early development of the flow for very large Rayleigh numbers which should reveal a flow pattern that is more consistent with that observed in our climate system which consists of three primary counterrotating circulation cells known as Hadley, Ferrel and Polar cells.

Acknowledgements

Financial support for this research was provided by the Natural Sciences and Engineering Research Council of Canada and the Faculty of Mathematics at the University of Waterloo.

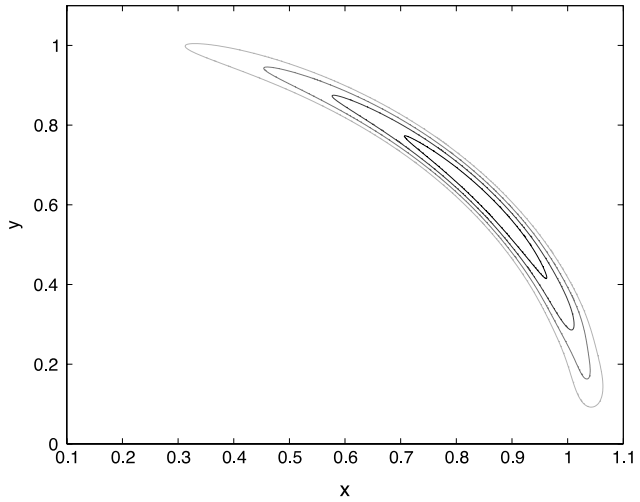

Fig. 9. Streamline circulation pattern in Cartesian coordinates at time $t = 8.5$. Parameter values: $Ra = 1890$, $\delta = 0.1$, $\gamma = 0.5$, $Pr = 0.7$, $Ro = 1$.

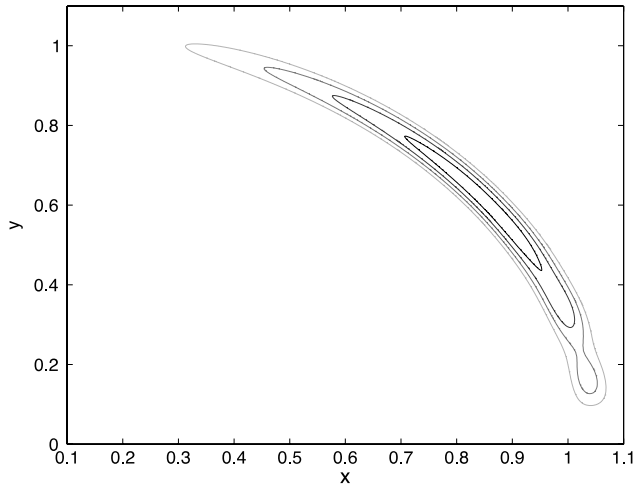

Fig. 10. Streamline circulation pattern in Cartesian coordinates at time $t = 10.7$. Parameter values: $Ra = 1890$, $\delta = 0.1$, $\gamma = 0.5$, $Pr = 0.7$, $Ro = 1$.

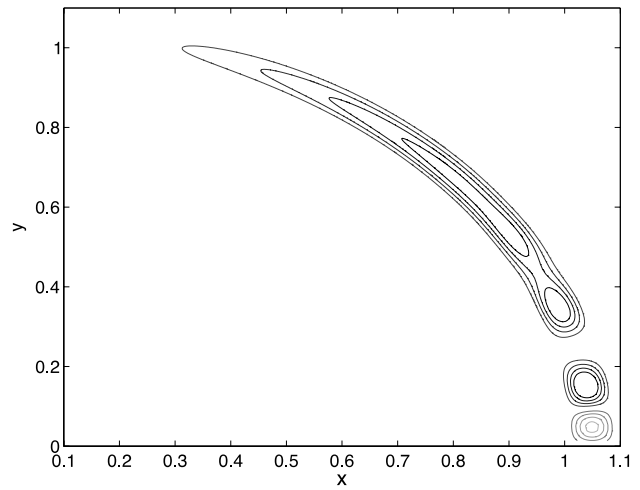

Fig. 11. Streamline circulation pattern in Cartesian coordinates at time $t = 12.9$. Parameter values: $Ra = 1890$, $\delta = 0.1$, $\gamma = 0.5$, $Pr = 0.7$, $Ro = 1$.

Appendix A. Primitive variable formulation

Here we present the Navier–Stokes and energy equations in dimensional form expressed in terms of the velocity and pressure. For a Boussinesq fluid in a rotating reference frame these equations cast in vector form are given by [23]

$$\vec{\nabla}\cdot\vec{v}=0, \tag{A.1}$$

$$\frac{\partial\vec{v}}{\partial t}+(\vec{v}\cdot\vec{\nabla})\vec{v}+2\vec{\Omega}\times\vec{v}=-\frac{1}{\rho_r}\vec{\nabla}P'+\alpha[g(r)\hat{\vec{e}}_r+\vec{\Omega}\times(\vec{\Omega}\times\vec{r})](T-T_r)+\nu\nabla^2\vec{v}, \tag{A.2}$$

$$\frac{\partial T}{\partial t}+(\vec{v}\cdot\vec{\nabla})T=\kappa\nabla^2T. \tag{A.3}$$

In the above $\vec{r}$ is the position vector and $\vec{v}$ represents the fluid velocity in a frame of reference that is rotating about the polar axis at a rate $\Omega=|\vec{\Omega}|$ where

$$\vec{\Omega}=\Omega(\cos\theta\hat{\vec{e}}_r-\sin\theta\hat{\vec{e}}_\theta),$$

and $\hat{\vec{e}}_r,\hat{\vec{e}}_\theta$ are unit vectors in the radial and latitudinal directions, respectively. T denotes the temperature and P' refers to the pressure deviation from P_0 where P_0 satisfies

$$\frac{1}{\rho_r}\vec{\nabla}P_0+g(r)\hat{\vec{e}}_r+\vec{\Omega}\times(\vec{\Omega}\times\vec{r})=\vec{0}.$$

It follows that

$$P'=P_0-\frac{\rho_r g_0R^2}{r}-\frac{\rho_r\Omega^2}{2}r^2\sin^2\theta.$$

Here,

$$g(r)=g_0\left(\frac{R}{r}\right)^2,$$

is the acceleration due to gravity with g_0 denoting the value on the surface, and R is the radius of the sphere. For a Boussinesq fluid the density varies according to

$$\frac{\rho}{\rho_r}=1-\alpha(T-T_r),$$

where ρ_r represents the reference density corresponding to temperature T_r. All other fluid properties (i.e. ν,κ) are assumed to remain constant.

For flow possessing both azimuthal and equatorial symmetry the continuity equation (A.1) in spherical coordinates can be written as

$$\frac{\partial}{\partial r}\left(r^2\sin\theta v_r\right)+\frac{\partial}{\partial\theta}\left(r\sin\theta v_\theta\right)=0,$$

where v_r, v_θ are the velocity components in the r,θ directions, respectively. This equation will automatically be satisfied if we introduce a meridional stream function defined by

$$v_r=\frac{1}{r^2\sin\theta}\frac{\partial\psi}{\partial\theta},\qquad v_\theta=-\frac{1}{r\sin\theta}\frac{\partial\psi}{\partial r}. \tag{A.4}$$

The pressure can be eliminated by forming the vorticity transport equation by taking the curl of Eq. (A.2). If we let $\vec{\zeta}=\vec{\nabla}\times\vec{v}$ and invoke vector identities, this leads to

$$\frac{\partial\vec{\zeta}}{\partial t}+(\vec{v}\cdot\vec{\nabla})\vec{\zeta}-2(\vec{\Omega}\cdot\vec{\nabla})\vec{v}-(\vec{\zeta}\cdot\vec{\nabla})\vec{v}=-\frac{\alpha g_0}{r}\frac{\partial T}{\partial\theta}\hat{\vec{e}}_\phi+\nu\nabla^2\vec{\zeta}, \tag{A.5}$$

where $\hat{\vec{e}}_\phi$ is the unit vector in the azimuthal direction. Here, we have made the approximation $g(r)\hat{\vec{e}}_r+\vec{\Omega}\times(\vec{\Omega}\times\vec{r})\approx g_0\hat{\vec{e}}_r$ where the term $\vec{\Omega}\times(\vec{\Omega}\times\vec{r})$ represents the centrifugal acceleration. For a thin spherical shell of thickness $H\ll R$ that is not rapidly rotating this is an excellent approximation. Making use of (A.4), the azimuthal component of Eq. (A.2) is given by

$$\begin{aligned}&\frac{\partial v_\phi}{\partial t}+\frac{1}{r^2\sin\theta}\frac{\partial\psi}{\partial\theta}\frac{\partial v_\phi}{\partial r}-\frac{1}{r^2\sin\theta}\frac{\partial\psi}{\partial r}\frac{\partial v_\phi}{\partial\theta}\\&\quad=\frac{1}{r^3\sin^2\theta}(v_\phi-2\Omega\sin\theta)\left(r\cos\theta\frac{\partial\psi}{\partial r}-\sin\theta\frac{\partial\psi}{\partial\theta}\right)+\nu\left(\nabla^2v_\phi-\frac{v_\phi}{r^2\sin^2\theta}\right),\end{aligned} \tag{A.6}$$

while the azimuthal component of Eq. (A.5) becomes

$$\frac{\partial \zeta_\phi}{\partial t} + \frac{1}{r^2 \sin\theta}\frac{\partial \psi}{\partial \theta}\frac{\partial \zeta_\phi}{\partial r} - \frac{1}{r^2 \sin\theta}\frac{\partial \psi}{\partial r}\frac{\partial \zeta_\phi}{\partial \theta} + \frac{\alpha g_0}{r}\frac{\partial T}{\partial \theta}$$
$$= \frac{2}{r^2 \sin\theta}\left(\frac{W}{r^2 \sin^2\theta} + \Omega\right)\left(r\cos\theta\frac{\partial W}{\partial r} - \sin\theta\frac{\partial W}{\partial \theta}\right) + \nu\left(\nabla^2\zeta_\phi - \frac{\zeta_\phi}{r^2\sin^2\theta}\right), \tag{A.7}$$

where ζ_ϕ denotes the azimuthal component of vorticity and $W = r\sin\theta v_\phi$ is the scaled zonal velocity with v_ϕ referring to the azimuthal, or zonal, velocity component. Following [24], we introduce the scaled vorticity, ω, which is related to ζ_ϕ through the relation $\omega = r\sin\theta\zeta_\phi$. In this investigation we work in terms of the flow variables ψ, ω, W and T. In terms of these variables and cast in dimensionless form the stream function Eq. (1) follows directly from the relation $\zeta_\phi = [\vec{\nabla}\times\vec{v}]_\phi$, Eq. (A.7) transforms to Eq. (2), Eq. (A.6) produces Eq. (3), while Eq. (A.3) becomes Eq. (4). An advantage of working in terms of these variables is that it reduces the number of equations from five to four. Although the introduction of the vorticity presents complications associated with the lack of boundary conditions, working with the pressure also presents challenges.

Appendix B. Supplementary data

Supplementary material related to this article can be found online at http://dx.doi.org/10.1016/j.cam.2015.03.025.

References

[1] J. Coiffier, Fundamentals of Numerical Weather Prediction, Cambridge University Press, Cambridge, 2011.
[2] J.P. Peixoto, A.H. Oort, Physics of Climate, American Institute of Physics, New York, 1992.
[3] A. Kasahara, Various vertical coordinate systems used for numerical weather prediction, Mon. Weather Rev. 102 (1974) 509–522.
[4] T.J. Phillips, et al., Evaluating parameterizations in General Circulation Models, climate simulation meets weather prediction, Amer. Meteor. Soc. (2004) 1903–1915.
[5] P.S. Marcus, L.S. Tuckerman, Simulation of flow between concentric rotating spheres, part 1: steady states, J. Fluid Mech. 185 (1987) 1–30.
[6] P.S. Marcus, L.S. Tuckerman, Simulation of flow between concentric rotating spheres, part 2: transitions, J. Fluid Mech. 185 (1987) 31–65.
[7] P. Chossat, G. Iooss, The Couette–Taylor Problem, Springer-Verlag, New York, 1994.
[8] J.E. Hart, G.A. Glatzmaier, J. Toomre, Space-laboratory and numerical simulations of thermal convection in a rotating hemispherical shell with radial gravity, J. Fluid Mech. 173 (1986) 519–544.
[9] V. Lesueur, A. Abouelainine, A. Mangeney, P. Drossart, Geostrophic motions of a Boussinesq fluid in a thick rotating spherical shell, Geophys. Astrophys. Fluid Dyn. 91 (1999) 1–43.
[10] S. Chandrasekhar, Hydrodynamic and Hydromagnetic Stability, Dover Publications, New York, 1981, (first published 1961, Oxford University Press).
[11] I.C. Walton, The effects of slow spatial variations on Bénard convection, Quart. J. Mech. Appl. Math. 35 (1982) 33–48.
[12] H. Bénard, Les tourbillons cellulaires dans une mappe liquide, Rev. Gen. Sci. Pures Appl. 11 (1900) 1261–1271.
[13] P.G. Drazin, W.H. Reid, Hydrodynamic Stability, second ed., Cambridge University Press, Cambridge, 2004.
[14] E. Bodenschatz, W. Pesch, G. Ahlers, Recent developments in Rayleigh–Bénard convection, Annu. Rev. Fluid Mech. 32 (2000) 709–778.
[15] A.M. Soward, C.A. Jones, The linear stability of the flow in the narrow gap between two concentric rotating spheres, Quart. J. Mech. Appl. Math. 36 (1983) 19–42.
[16] G.M. Lewis, W.F. Langford, Hysteresis in a rotating differentially heated spherical shell of Boussinesq fluid, SIAM J. Appl. Dyn. Syst. 7 (2008) 1421–1444.
[17] A. Barrow, S.J. Garrett, N. Peake, Global linear stability of the boundary-layer flow over a rotating sphere, Eur. J. Mech. B Fluids 49 (2015) 301–307.
[18] S.J. Garrett, N. Peake, The stability and transition of the boundary layer on a rotating sphere, J. Fluid Mech. 456 (2002) 199–218.
[19] R.J. Leveque, Finite Difference Methods for Ordinary and Partial Differential Equations: Steady-State and Time-dependent Problems, Society for Industrial and Applied Mathematics, Philadelphia, 2007.
[20] S.C.R. Dennis, L. Quartapelle, Some uses of Green's theorem in solving the Navier–Stokes equations, Internat. J. Numer. Methods Fluids 9 (1989) 871–890.
[21] P.M. Gresho, Incompressible fluid dynamics: some fundamental formulation issues, Annu. Rev. Fluid Mech. 23 (1991) 413–453.
[22] H. Huang, B.R. Seymour, The no-slip boundary condition in finite difference approximations, Internat. J. Numer. Methods Fluids 22 (1996) 713–729.
[23] J. Pedlosky, Geophysical Fluid Dynamics, Springer-Verlag, Berlin, New York, 1987.
[24] S. Goldstein (Ed.), Modern Developments in Fluid Dynamics, Clarendon Press, Oxford, 1938, p. 115.